Solubility of platinum-arsenide melt and sperrylite in synthetic basalt at 0.1 MPa and 1200°C with implications for arsenic speciation and platinum sequestration in mafic igneous systems

Canali, A.C[1]., Brenan, J.M.[2] and Sullivan, N.A.[3]

1) Department of Earth Sciences, Memorial University of Newfoundland, St. John's, NL, Canada

2) Department of Earth Sciences, Dalhousie University, Halifax, NS, Canada

3) Department of Earth Sciences, University of Toronto, Toronto, ON, Canada

Abstract

To better understand the Pt-As association in natural magmas, experiments were done at 1200°C and 0.1 MPa to measure the solubility of Pt and Pt-arsenide phases (melt and sperrylite, $PtAs_2$), as well as to determine the oxidation state, and identify evidence for Pt-As complexing, in molten silicate. Samples consisting of synthetic basalt contained in chromite crucibles were subject to three experimental procedures. In the first, platinum solubility in the synthetic basalt was determined without added arsenic by equilibrating the sample with a platinum source (embedded wire or bead) in a gas-mixing furnace. In the second, the sample plus a Pt-arsenide source was equilibrated in a vacuum-sealed fused quartz tube containing a solid-oxide oxygen buffer. The third approach involved two steps: first equilibrating the sample in a gas-mixing furnace, then with added arsenide melt in a sealed quartz tube. Oxygen fugacity was estimated in the latter step using chromite/melt partitioning of vanadium.

Method two experiments done at high initial arsenic activity (PtAs melt + $PtAs_2$), showed significant loss of arsenic from the sample, the result of vapour transfer to newly-formed arsenide phases in the buffer. Method three experiments showed no loss of arsenic, yielding a uniform final distribution in the sample. Analyses of run-product glasses from experiments which did not show arsenic loss reveal significant increase in arsenic concentrations with fO_2, varying from ~10 ppm (FMQ-3.25) to >10,000 ppm (FMQ+5.5). Despite very high arsenic loadings (>1000 ppm), the solubility of Pt is similar in arsenic-bearing and arsenic-free glasses. The variation in arsenic solubility

32 with fO_2 shows a linear relationship, that when corrected for the change in the activity of

33 dissolved arsenic with the melt ferric/ferrous ratio, yields a solubility-fO_2 relationship

34 consistent with As^{3+} as the dissolved species. This result is confirmed by x-ray

35 absorption near edge structure (XANES) determination on run-product glasses.

36   Levels of arsenic required for Pt-arsenide saturation are 50-500 ppm over the fO_2

37 range of most terrestrial basalts (FMQ to FMQ-2), >100x higher than the arsenic

38 concentrations typical of such magmas, indicating significant enrichment of arsenic is

39 required if Pt-arsenide saturation is to occur. In contrast, the level of dissolved Pt

40 required to saturate in sperrylite is >8x lower than for pure Pt, suggesting that arsenic

41 enrichment could lead to Pt removal at concentrations much less than required for pure

42 metal saturation.

43

44   **Keywords**: arsenic, platinum, sperrylite, solubility

45

46 **Introduction**

47   Although sulfur has long been implicated as an important ligand in the

48 concentration of the platinum group metals (PGE) at the magmatic stage, there is

49 evidence to suggest that arsenic could also play a significant role in some cases. For

50 example, close textural relations between relatively PGE-depleted base metal sulfide and

51 coexisting PGE-rich arsenide phases (NiAs, nickeline; $Ni_{11}As_8$, maucherite; NiAsS,

52 gersdorffite), interpreted to have been coexisting immiscible sulfide and arsenide melts,

53 have been reported in the magmatic sulfide segregations within the Ronda and Beni

54 Besoura peridotite bodies (Gervilla et al., 1996; Pina et al., 2013), the Kylmakoski

55 (Finland) Ni-Cu deposit (Gervilla et al., 1998) and komatiite-hosted base metal sulfide

56 mineralization (Dundonald Beach South, Ontario (Hanley, 2007); Rosie Ni Prospect,

57 Western Australia (Godel et al., 2012)). Recent work on samples from Creighton Mine,

58 Sudbury (Dare et al., 2010) have shown that the base metal sulfides are not the dominant

59 hosts for some PGE, and that Ir, Rh, Pt occur as arsenic-rich discrete platinum group

60 minerals (PGMs; i.e., irarsite-hollingsworthite, IrAsS-RhAsS; sperrylite, $PtAs_2$), possibly

61 crystallizing before or with early-formed magmatic sulfide minerals (e.g., monosulfide

62 solid solution, or MSS). Detailed chemical imaging has also revealed textural evidence

63 favouring the direct crystallization of Pt-Fe alloy along with sperrylite from the magma

64 that formed the orthopyroxenite section of the Monts de Cristal Complex (Gabon; Maier

65 et al., 2015; Barnes et al 2016).

66 　　　　Past experimental work to explore the arsenic-PGE magmatic association has

67 largely focused on behaviour related to the crystallization of sulfide liquid. The existence

68 of S-bearing but arsenic-rich liquids is described by Skinner et al. (1976) who measured

69 an extensive two-liquid field in the system Pd-As-S at 1000°C and 0.1 MPa. Helmy et al.

70 (2013b) showed that similar phase relations extend into systems with Fe and Ni, with Pd-

71 As-rich liquids stable to 770°C (and possibly below) at 0.1 MPa, with a strong preference

72 of Ni over Fe relative to coexisting sulfide melt. Experiments on the Pt-As-S system

73 (Skinner et al., 1976; Mackovicky et al., 1990; 1992) document extensive solid solution

74 between As-S melts, and that sperrylite is a possible early-formed phase, although the

75 minimum As content of the As-S liquid coexisting with sperrylite at 1000°C is quite high

76 (several wt%). Helmy et al. (2013) showed that the addition of Fe (and Ni) to this system

77 significantly reduces the solubility of sperrylite in the sulfide melt to values ranging from

78 9400 ppm at 1150°C to 6200 ppm at 770°C. Similarly, Helmy et al. (2013) determined

79 that the arsenic content of sulfide melt coexisting with Pd-Ni-rich arsenide melts varies

80 from 37800 ppm at 1150°C to ~400 ppm at $770\ ^{\circ}$C. Such high As solubility in molten

81 sulfide would suggest that sperrylite or Pd-Ni-As bearing melt is not likely to form early

82 in the magmatic sulfide crystallization sequence unless the system has acquired unusually

83 high As levels. Synukova and Kosyakova (2012) investigated the conditions of

84 formation for the Ir and Rh-bearing sulfarsenides of the irarsite-hollingsworthite series in

85 dynamic crystallization experiments, indicating these phases can form near the sulfide

86 liquidus, although detailed information on the As concentrations required for saturation

87 were not provided. Empirical observations (Hanley, 2007; Pina et al., 2013) suggest that

88 the PGEs will be preferentially concentrated in the arsenide phase. Pina et al. (2013)

89 reconstructed sulfide and arsenide liquid compositions in samples from the Beni Bousera

90 magmatic Cr-Ni mineralization (Morocco), and determined values of $D^{AsLiq/SulfLiq}$ of

91 ~100 for the PGEs. Hanley (2007) estimated relative arsenide-sulfide partitioning by

92 comparing concentrations (on a 100% sulfide basis) between an As-rich high grade lens,

93 with lower grade As-poor segregations, occurring in a series of mineralized komatiite

94 flows. The arsenic-rich high grade lens was found to be enriched by ~7-60x for Pt and

95 Pd..

96   In contrast to the body of experimental and empirical work on sulfide systems,

97 comparatively little information is available to evaluate the conditions for saturation in

98 PGE-bearing arsenide phases in molten silicate. Preliminary measurements of the

99 solubility of molten Fe-As-S in basalt melt at 1200°C and 1 GPa (fO$_2 \leq$ FMQ buffer;

100 summarized in Brenan et al., 2016, section entitled "Role of the chalcogens (Se, Te, As,

101 Bi, Sb)) have revealed values of 1100 and 3300 ppm, for silicate melts with ~19 and ~13

102 wt% FeO, respectively. How much these values change with other intensive parameters,

103 such as oxygen fugacity and temperature, is unknown. Moreover, there is a complete

104 lack of information on the conditions for direct crystallization of arsenic-bearing

105 minerals, such as the irarsite-hollingsworthite series, and sperrylite. Such information is

106 essential, however, to fully evaluate the possible role of these phases in the early

107 sequestration of the PGEs, as well as to understand how these elements may become

108 fractionated from each other. In this paper, the results of experiments to measure the As

109 and Pt content of synthetic basalt at saturation in various Pt-As phases (Pt-As melt and

110 sperrylite) is presented. The effect of oxygen fugacity on this behaviour is explicitly

111 evaluated, with results providing information on the speciation of arsenic in silicate melt,

112 as well as the conditions required for magmatic crystallization of sperrylite.

113

114 **Experimental Methods**

115 **Overview** The goal of the experiments was to saturate synthetic basalt with a Pt-

116 arsenide-bearing phase assemblage over a range of fO$_2$, so as to establish solubility

117 systematics that could be applied to natural magmatic systems. A fundamental challenge

118 to the arsenic-bearing experiments is the volatility of arsenic at high temperature, met in

119 this case through the use of fused quartz ampoules to contain samples. In that approach,

120 initial experiments involved the use of internal solid oxide buffers to fix oxygen fugacity.

121 Owing to loss of arsenic from the sample to the buffer, subsequent experiments were

122 done without the buffer, but pre-equilibrated in a gas-mixing furnace. In order to

123 establish a "baseline" to determine the effect of dissolved arsenic on Pt metal solubility, a

124 series of experiments was also done at variable fO$_2$ under arsenic-free conditions.

4

125   Details of these methods are provided below, and a summary of experiments and run

126   conditions is provided in Table 1.

127

128   **Silicate melt synthesis** All experiments were done with the same Fe-bearing basalt

129   analogue (hereafter, silicate melt), synthesized by initial calcining of a powdered, high

130   purity oxide mix, followed by fusion at 1400°C for 30 minutes, then a final grinding. For

131   initial experiments (Sp7, Sp11, Sp12, Sp14), the oxide mix was fused in air. However,

132   previous work (Bennett et al., 2014; Medard et al 2016), has shown that the occurrence of

133   undissolved Pt nanoparticles in more reduced experiments (Ni-NiO buffer and below)

134   was significantly less if glasses contained a low ferric iron component initially. So as to

135   limit the introduction of ferric iron, subsequent experiments were done using a silicate

136   melt starting material that had been fused in a gas-mixing furnace at an fO_2 equal to the

137   FMQ buffer. All glass compositions were fused in high purity alumina crucibles, rather

138   than Pt, so as to prevent the introduction of Pt nanoparticles.

139

140   **Platinum solubility measurements, no As** Arsenic-free platinum solubility experiments

141   were done by encapsulating the silicate melt (~20 milligrams), along with a 0.2 mm Pt

142   wire or bead, in crucibles made from natural adcumulate chromitite (Royal Ontario

143   Museum reference M4557; ~5 mm long x ~5 mm outer diameter x ~2 mm inner

144   diameter). Samples were equilibrated at 1200°C for 46-96 hours (most 90-96 hours) with

145   fO_2 controlled by either gas-mixing or using solid oxide buffers. The latter method was

146   used to assess if different buffering methods affects experimental results. Gas mixing

147   experiments were done using a vertical tube furnace, employing CO-CO_2 mixtures, with

148   fO_2 confirmed before and after the experiment with a Y-doped zirconia sensor

149   (Australian Oxytrol Systems). Experiments were terminated by rapidly lowering the

150   sample to the sealed cold end of the furnace for quenching while still in the buffering gas

151   stream. Experiments using solid buffers for fO_2 control were done using vacuum-sealed

152   fused quartz ampoules. The solid buffer mixture (~100 milligrams of a 1:1 mix of either

153   Mo-MoO_2, MnO-Mn_3O_4 or Ni-NiO) was loaded into the bottom of the open ampoule (5

154   mm inner diameter, 9 mm outer diameter), followed by a layer of powdered silica, the

155   chromite crucible, a thin (< 1mm thick) fused silica ring, and finally a solid fused silica

5

156   spacer on top. The purpose of the ring is to prevent melt from wicking out of the crucible

157   as a result of contact with the solid spacer, since this usually leads to contamination and

158   failure of the ampoule wall (the reader is referred to Figure 2 of Mungall and Brenan

159   (2014) for images of the silica ampoule configuration). The loaded ampoule was then

160   evacuated for 30 minutes or more, and fused shut with an oxyacetylene torch. Samples

161   were placed upright on the hearthplate of a glass-melting furnace, and held for the run

162   duration, with experiments terminated by dropping the sample into an ice-water bath.

163   Solid buffer phase assemblages were confirmed by visual inspection and x-ray

164   diffraction.

165

166   **Solubility of Pt-arsenide** Initial experiments to determine the solubility of sperrylite and

167   Pt-arsenide melt were done using fused quartz ampoules in the identical fashion as those

168   to measure Pt solubility. The only modification was the substitution of the Pt wire or

169   bead by a fragment of Pt-arsenide. The initial phase assemblage of the Pt-arsenide

170   comprised sperrylite ($PtAs_2$) + quenched PtAs melt, synthesized using a bulk

171   composition of ~60:40 Pt:As by mass, guided by the Pt-As phase diagram (Okamoto,

172   1990). This material was synthesized by annealing the appropriate mixture of Pt and As

173   powders in a vacuum-sealed fused quartz ampoule at 500°C for 4 hours, then heating to

174   900°C over 4 hours, holding for 24 hours, then removal from the furnace and cooling in

175   air.

176   Subsequent solubility experiments revealed significant loss of arsenic from the Pt-

177   arsenide source, resulting in the final assemblage of Pt + Pt-As melt (experiments at Mo-

178   MoO_2, Ni-NiO) or just Pt (experiments at MnO-Mn_3O_4). Inspection of the buffers from

179   these experiments revealed the presence of arsenide-bearing phases (Mo_2As, solid NiAs,

180   Mn-O-As melt), confirming the likely transfer, via a vapour phase, of arsenic sourced

181   from the Pt-arsenide to the solid buffer sink. Despite the apparent failure of this method,

182   results from two of these experiments are reported here (Sp7 and Sp14), done with the

183   MnO-Mn_3O_4 buffer, as each yielded a homogeneous distribution of Pt in the silicate

184   melt, and wt% levels of As, despite some loss to the buffer. Data provided from this

185   experiment help to evaluate the effect of unusually high loading of arsenic in the silicate

186   melt on Pt solubility.

187   With this experience of As-loss to the solid buffer, most subsequent experiments

188   were done buffer-free, but with the fO_2 monitored using the vanadium content of run-

189   product glasses (see below for details). The buffer-free experiments were done in two

190   steps. First, the silicate melt + Pt source was loaded into a chromite crucible, then

191   equilibrated either in a gas-mixing furnace or in a fused quartz ampoule containing solid-

192   oxide buffers at 1200°C for 96 hours. The chromite crucible was then recovered and a

193   few milligrams of the Pt-arsenide source was placed in contact with the quenched silicate

194   melt. The sample was reinserted into a fused quartz ampoule and vacuum-sealed. In

195   principle, the redox state of the sample in this second stage of the experiment is imposed

196   by the ferric/ferrous ratio of the silicate melt and chromite, as fixed in the first stage.

197   However, other factors come into play, most notably the quality of the vacuum when the

198   sample was sealed, as well, evidence suggests the dissolution of Pt-arsenide in the silicate

199   melt involves the consumption of oxygen (see below). With the exception of experiment

200   M2-SP6, run products from stage 2 were slightly to significantly more oxidized than the

201   fO_2 imposed in stage 1 (Table 1), suggesting variable quality of the vacuum prior to

202   sealing in stage 2. The reduction of M2-SP6 by ~1 log unit in fO_2 likely reflects a

203   reasonably good vacuum, and the arsenide dissolution effect.

204

205   **Reduced single-stage experiment** Despite multiple attempts, it was not possible to do a

206   successful two-stage experiment at conditions more reduced than the Ni-NiO buffer, due

207   to an inability to achieve a vacuum low enough for the required partial pressure of

208   oxygen. As an alternative, a single stage experiment under reducing conditions was done

209   with a slightly modified technique to inhibit arsenic loss. In this case, the added Pt-

210   arsenide phase assemblage was Pt + PtAs melt, synthesized as per the $PtAs_2$-PtAs melt

211   starting material, but using an As-poor bulk composition. The Pt-PtAs melt assemblage

212   imposes a lower arsenic activity on the system. This experiment was buffered with the

213   assemblage Mo + MoO_2, employing the same sample + buffer configuration as described

214   previously. Unlike the previous experiments using the Mo-MoO_2 assemblage, however,

215   this run-product buffer did not contain any detectable Mo-arsenide. This is consistent

216   with the lower initial As activity of the Pt-PtAs melt assemblage, which was insufficient

217   to form Mo_2As in the buffer, thus preventing the loss of arsenic seen in the experiments

7

218   with the $PtAs_2$-PtAs melt assemblage. The resulting silicate glass had an arsenic level

219   similar to glasses produced in equivalent single-stage experiments at the Mo-MoO_2

220   buffer using the $PtAs_2$-PtAs melt source, but unlike the previous results, the arsenic

221   content was uniform.

222

223   **Estimation of sample fO_2 in 2-stage experiments** Vanadium can exist in silicate melt

224   with oxidation states ranging from 2+ to 5+, depending on fO_2, resulting in changes in

225   the bulk mineral/melt partitioning behaviour (Canil, 1997; Canil & Fedortchouk, 2001;

226   Mallmann and O'Neill, 2009). In the current study, it was found that the vanadium

227   content of the chromite used for sample encapsulation is remarkably uniform (~ 880 ± 40

228   ppm, n = 7 samples), and owing to the large crucible to melt ratio in experiments, the

229   capsule effectively buffers the vanadium content of the melt. It has been shown that the

230   spinel/melt partitioning (D_V) of the different vanadium valence states changes in the

231   order: $D_V^{2+} > D_V^{3+} > D_V^{4+} > D_V^{5+}$ (Mallman and O'Neill, 2009), hence, changes in the

232   vanadium content of the run-product melt reflects the fO_2 of the system. The relation

233   between vanadium concentration in the silicate melt and fO_2 was therefore calibrated

234   using the buffered (but As-free) experiments from this study, yielding the relation:

235

236    $\log V \text{ (ppm)} = 4.30 + 0.510 (\log fO_2) + 0.0197 (\log fO_2)^2$ (1)

237

238   (n = 5 experiments; r = 0.99957).

239

240   In previous work using a similar capsule arrangement (Mungall and Brenan, 2014), fO_2 is

241   calculated using the melt Cr content, which is only calibrated over a limited range of fO_2

242   (FMQ-2 to +1.6), considerably less than the ~8 orders of magnitude range determined

243   here. Values of fO_2 reported for stage 2 of the two-stage experiments are therefore based

244   on the vanadium calibration, which is considered to be more accurate.

245

246   **Analytical Methods**

247   **Electron microprobe analysis** Run products were mounted in 1" diameter molds and

248   backfilled with epoxy, then ground and polished for textural and elemental analysis.

249 Major element analysis was performed using the Cameca SX50 or subsequently, JEOL

250 JXA8230, electron microprobes at the University of Toronto. Analytical conditions were

251 15 kV accelerating voltage and a beam current of 10 nA for glass or 20 kV and 40 nA for

252 alloy or arsenide. A defocused beam (10-30 microns) was used to analyze the silicate and

253 arsenide phases. Owing to the coarse nature of the quenched arsenide melt, some

254 experiments were analysed by semi-quantitative EDS using a rastered electron beam

255 incorporating at least a 30 x 30 micron area. The accuracy of this method was verified by

256 analysing synthetic sperrylite (PtAs$_2$), which returned a result within error of that defined

257 by mineral stoichiometry. The Pt-Fe alloys produced in experiments were measured

258 using a 20 kV accelerating voltage, 50 nA beam current and a focused electron beam.

259 Standards for silicate analysis were natural basalt glass (Si, Al, Mg, Fe, Ca), albite (Na),

260 orthoclase (K), bustamite (Mn), and arsenopyrite (As). Standards for analysis of alloys

261 and arsenides were pure Fe and Pt metals and arsenopyrite (As). For all analyses, raw

262 count rates were converted to concentrations using a modified ZAF data reduction

263 scheme.

264

265 **Laser ablation ICP-MS analysis**   Trace elements were determined using the laser

266 ablation ICP-MS facility in the Department of Earth Sciences at the University of

267 Toronto. This system employs a frequency quintupled Nd:YAG laser operating at 213

268 nm, coupled to a VG PQ Excell quadrupole mass spectrometer with He flushing the

269 ablation cell to enhance sensitivity (Eggins et al., 1998). Silicate glasses were analysed

270 using a laser repetition rate of 10 Hz and a spot size of 40-100 microns. Beam irradiance

271 was optimized for each material depending on photon-coupling characteristics. Factory-

272 supplied time resolved software was utilized for the acquisition of individual analyses. A

273 typical analysis involved 20 seconds of background acquisition with the ablation cell

274 being flushed with He, followed by laser ablation for 60 seconds. Analyses were

275 collected in a sequence, with the first and last four spectra acquired on standards. At least

276 four analyses were done on glasses from each experiment. Data reduction was done off-

277 line using the GLITTER version 5.3 software package, supplied by Macquarie Research,

278 Ltd. Time-resolved spectra were evaluated individually for Pt homogeneity, and

279 inclusion "spikes" avoided when selecting regions for abundance determination. For

280   glasses in which nanonugget contamination was significant, only the lowest Pt

281   concentration is reported. Concentrations of V, As and Pt in the silicate glass were

282   quantified using the NIST 610 silicate glass, which contains 325 ppm As, 450 ppm V and

283   3.12 ppm Pt (Jochum et al., 2011). Ablation yields in glass were corrected by referencing

284   to the known concentration of Ca as determined by electron microprobe analyses. The

285   following isotopes were measured, with those in italics used for quantification: ^{43}Ca, ^{51}V,

286   ^{75}As, ^{194}Pt, ^{195}Pt.

287

288   **Synchrotron-based spectroscopy**   The X-ray absorption near-edge structure (XANES)

289   of the As $L_{2,3}$-edge for silicate glasses from experimental run-products and As-bearing

290   reference standards (As_2O_3, As_2S_3, $Ca_3(AsO_4)_2$, KH_2AsO_4, NiAs) were collected over

291   the energy range of 1300 to 1380 eV using the Spherical Grating Monochromator (SGM)

292   11ID-1 beamline (Regier et al. 2007) at the Canadian Light Source (CLS) synchrotron

293   (Saskatoon, Canada). The storage ring operates at an energy of 2.9 GeV, generates a 250

294   mA current, which decays to 160 mA between injection refills every 12 hours. XANES

295   analyses of glasses from experimental run-products were done on the "as mounted"

296   material, whereas the As-bearing reference standards were in powdered form. Analyses

297   were carried out simultaneously in both total electron yield (TEY) and fluorescence yield

298   (FY) modes, although only the FY spectra is reported. The beam spot size was

299   approximately 50 µm x 50 µm with an X-ray photon flux of ~1011 γ/s/0.1%BW and an

300   energy resolution of ±0.05 eV. The silicate glasses and As-bearing standards were

301   analyzed in the beamline end station under ultra-high vacuum (UHV) pressures in the

302   10^{-6} Torr range. The SGM beamline is equipped with four silicon-drift detectors (SDD)

303   which are specifically located at a large angle to the incident beam to reduce self

304   absorption of X-ray photons (Moulton et al. 2016). The electron binding energies for As

305   L_2-edge and As L_3-edge are 1359.1 eV and 1323.6 eV, respectively. The As L_3-edge

306   peak is vulnerable to interference from the Mg K-edge (1303 eV), however the As L_3-

307   peak is still resolved in silicate glasses with greater than 1 wt. % As. XANES As $L_{2,3}$-

308   edge spectra data was processed using the Athena software package (Ravel and Newville

309   2005). Silicate glass samples and As-bearing reference standards were each scanned 20

310   times over the energy range of 1300 to 1380 eV. The spectra were normalized to the

311   incident beam intensity (I_0) and spectra from all four SDD were averaged, with the

312   background subsequently removed.

313

314   **Results**

315   **Run-product arsenide textures and phase compositions**

316   Run-products consist of silicate melt, sparse crystals of plagioclase, as well as a Pt

317   or a Pt-As phase assemblage (Figure 1), depending on the starting composition and the

318   experiment mass balance. As-free experiments contained Pt-Fe alloy, whose iron content

319   is dictated by the fO_2 and the FeO content of the silicate melt (see Table 1). The PtAs

320   melt produced in experiments quenches to a fine-grained intergrowth of Pt + $PtAs_2$,

321   whose proportions depend on the bulk melt composition and subsequent quench

322   modification (Figure 1 b,c). The crystals of $PtAs_2$ produced in experiment M2SP8

323   (Figure 1c) are interpreted to have been stable at run conditions owing to their large size,

324   and generally euhedral habit. Dendritic growth of $PtAs_2$ on the margins of these crystals

325   likely formed on quench. The identity of the specific arsenide phase produced depends

326   on both mass balance and the starting material employed, as outlined in the methods

327   section. Some experiments done at oxidizing conditions contain wt% levels of arsenic

328   measured in the run-product glass. Despite such high arsenic loadings, the silicate melt

329   still quenches to a glass without visibly resolvable unmixing.

330   Based on the 0.1 MPa phase diagram for the Pt-As binary system (Okamoto,

331   1990; Figure 2), the eutectic melt composition is $Pt_{87}As_{13}$, the melt coexisting with Pt at

332   1200°C is $Pt_{92.5}As_{7.5}$ and the melt coexisting with $PtAs_2$ at 1200°C is $Pt_{77}As_{23}$ (all

333   compositions in wt%). The composition of PtAs melt coexisting with either Pt or $PtAs_2$

334   produced in all experiments is inconsistent with the phase diagram, with melt being

335   relatively Pt-poor coexisting with Pt, or Pt-rich coexisting with $PtAs_2$. This discrepancy

336   can be most readily attributed to the difficulty in quenching melts in this system, and

337   susceptibility to modification during the quenching process. Experiments involving

338   either two-phase assemblage show obvious signs of quench overgrowth on the stable

339   solid (e.g., Figure 1c), which would drive the residual melt composition away from the

340   equilibrium value and towards the eutectic composition. The observed sense of the shift

341   in composition is consistent with this effect (Figure 2). The composition of PtAs melt in

342   the one-phase field is predicted to range from $Pt_{92.5}As_{7.5}$ to $Pt_{77}As_{23}$, consistent with the

343   composition of single-phase melts produced under the most oxidising conditions (FMQ +

344   5.4-5.5). The single-phase melts produced in experiments at more reduced conditions

345   (FMQ + 0.7 to 3.6) are anomalously Pt-poor, having the composition $Pt_{74}As_{24-25}$,

346   consistent with $PtAs_2$ saturation as indicated by the phase diagram, although stable $PtAs_2$

347   crystals were not observed (Figure 2). PtAs melts produced at reduced conditions also

348   contain 0.25-1 wt% Fe. One possible reason for the discrepancy in phase assemblages is

349   that the dissolution of Fe into the arsenide melt at lower fO_2 conditions stabilizes melt,

350   relative to $PtAs_2$, in what would now be a ternary system.

351

352   **Approach to equilibrium**

353   The approach to equilibrium in experiments was judged by sample homogeneity

354   and the reproducibility of experiments done at similar conditions for different durations.

355   The time-resolved LA-ICPMS signal for arsenic was uniform in run-product glasses

356   (Figure 3), regardless of fO_2, implying the lack of undissolved micro- or nano-scale As-

357   bearing inclusions. As shown in Figure 4a, analytical traverses from near the glass-

358   vapour interface to the bottom of the sample capsule also reveal homogeneity for samples

359   synthesized over a large range in fO_2 (>8 orders of magnitude). Clear evidence for Pt

360   homogeneity is more limited, however (Figure 4b). For experiments done at fO_2

361   exceeding the Ni-NiO buffer ($\Delta FMQ = 0.68$), the time-resolved spectra for run-product

362   glasses was uniform (Figure 3), but with decreasing fO_2, increased sample heterogeneity

363   is evident, consistent with the presence of undissolved Pt inclusions. As such, the

364   reported Pt content of glasses from the low fO_2 (less than Ni-NiO) experiments is based

365   on integration of the lowest portion of the time-resolved signal, and is the lowest of the

366   glasses analyzed. In such case, the true Pt content is less than or equal to the reported

367   value. Hence, evidence for sample homogeneity is presented for samples displaying a

368   uniform time-resolved signal for Pt, corresponding to the high fO_2 (>Ni-NiO)

369   experiments (Figure 4b). As shown, the Pt concentrations vary by less than a factor of 2

370   (in the most extreme case), and are more typically within counting statistics. In addition

371   to the evidence for sample homogeneity, there is also good reproducibility in the Pt

372   content of experiments done for different durations. This is demonstrated by comparing

373   the results from the arsenic-free experiments PtSol21, 38, 39 (Table 1), done for 91, 95

374   and 46 hours at similar fO_2 (ΔFMQ of +5.17 to +5.27), in which the solubility of Pt was

375   measured to be 0.30 (0.07), 0.41 (0.03) and 0.35 (0.03) ppm, respectively.

376

377   **Platinum and arsenic solubility relations**

378   The variation in Pt concentration in the silicate melt as a function of oxygen

379   fugacity for experiments saturated in Pt-Fe alloy, Pt-As melt and sperrylite is portrayed in

380   Figure 5. Glass concentrations for experiments containing Pt-Fe alloy are normalized to

381   unit activity of platinum, using activity-composition relations in the alloy summarized by

382   Borisov and Palme (2000). The Pt solubility model determined by Ertel et al (1999)

383   involving the diopside-anorthite eutectic composition at 1300°C is also included for

384   reference (results from Borisov and Palme, 1997 are similar to Ertel et al, (1999) at high

385   fO_2). Results provide a baseline for comparison of the effect of arsenic on Pt solubility,

386   highlighting two important observations. First, Pt solubility measurements done with

387   arsenic dissolved in the silicate melt are generally similar to results for arsenic-free

388   compositions. This is especially evident for the two experiments done at relatively

389   oxidizing conditions (ΔFMQ + 4.3; Sp14 and Sp7) containing ~10,000 ppm As, and ~0.2

390   ppm Pt, which is similar to the value of ~0.1 ppm measured at the same fO_2 but without

391   arsenic (M2-Sp5). At more reduced conditions (ΔFMQ + 1.3; M2-Sp13), a similar result

392   is obtained, in which the Pt solubility is ~0.01 ppm, for a melt with ~800 ppm As,

393   compared to the interpolated As-free solubility of ~0.016 ppm. The second important

394   observation is that the Pt concentration in the silicate melt required for saturation in Pt-

395   arsenide phases (PtAs melt and sperrylite) is less than for pure Pt. This is consistent with

396   the lower Pt content of these phases, with the lowest solubility measured for sperrylite,

397   exhibiting an ~8-fold reduction compared to the case for pure Pt. These combined results

398   indicate that despite the dissolution of copious amounts of arsenic in the silicate melt, the

399   solubility of Pt is largely unaffected, except if a PtAs phase is stabilized, resulting in

400   saturation at a lower level of dissolved Pt.

401   In contrast to the very low concentrations of Pt measured in the silicate melt,

402   depending on fO_2, levels of dissolved As are >100- to >10,000-fold higher, and this holds

403   true regardless of the saturating arsenide phase (Table 1). For example, at FMQ-3, the

Results from XANES As $L_{2,3}$-edge

Previous studies investigating the valence state of As using XANES have usually examined the As K-edge at approximately 11867 eV (Morin et al. 2003; Thoral et al. 2005; Lowers et al. 2007; Borisova et al. 2010, Foster and Kim 2014). Alternatively, Benzerara et al. (2008) showed that the edge energy at the As $L_{2,3}$-edge is similarly dependent on valence state of As. Their study demonstrated that As^{3+} reference standards exhibit a single peak, whereas the As^{5+} reference standards demonstrate an additional peak (doublet) at 3.6 eV higher relative to As^{3+} reference standards. Our XANES As $L_{2,3}$-edge qualitatively show that the run-product spectra have comparable edge energies to the As(III) oxygen-bearing reference compound (As_2O_3) in the form of a single peak (Fig 6). This implies that the As is dissolved in the run-product glass as a trivalent cation. Similar to Benzerara et al. (2008), the spectra for As(V) oxygen-bearing reference compounds ($Ca_3(AsO_4)_2$ and KH_2AsO_4) demonstrate the development of a doublet and an increased edge energy by ~4 eV relative to As_2O_3, marked by the edge energy with higher amplitude. The As(III) sulfur-bearing reference compound (As_2S_3) exhibits an edge energy of ~2 eV lower than the As_2O_3 edge energy. Although As is known to be present as a trivalent cation in As_2S_3, variations in covalent bonding between As(III) sulfur-bearing and As(III) oxygen-bearing compounds has been shown in XANES As K-edge studies to have a small difference in edge energy for the same valence state (Lowers et al. 2007; Borisova et al. 2010). The spectra reported for anionic As in the form of Ni(II)As is not comparable to the run-product spectra and demonstrates a subtle rise in absorbance at ~1319 eV followed by a more pronounced rise in absorbance at ~1322 eV. Because the run-product glasses contain significant concentrations of MgO, the run-product spectra show a strong peak in absorbance at ~1306 eV due the presence of the Mg K-edge located ~30 eV before the As L_3-edge. The continuum signal for the Mg K-

435   edge has superimposed the absorbance of the As L_3-edge, consequently hindering the

436   true spectral shape and amplitude of the spectra. <mark>Hence, it is possible that the spectral</mark>

437   <mark>influence of small amounts of anionic As could be masked by this effect.</mark>

438

439   **Discussion**

440   **Interpretation of platinum solubility relations**

441   The solubility of Pt in Fe-free silicate melt compositions has been measured over

442   a similar range of fO$_2$ as reported here, but higher temperature, by Borisov and Palme

443   (1997) and Ertel et al (1999), with results consistent with Pt dissolving as a 2+ species in

444   the melt by the reaction:

445

446    $Pt_{metal} + 1/2O_2 = PtO_{melt}$ (2)
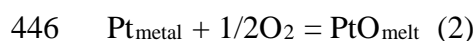
447

448   With an equilibrium constant, K$_2$, of the form:

449

450    $K_2 = [PtO_{melt}] / [Pt_{metal}]fO_2^{1/2}$ (3)

451

452   In which square brackets denote activities. For the case of pure Pt, equation 3 can be

453   linearized and solved for the concentration of Pt in the melt:

454

455    $Log (Pt, ppm) = \frac{1}{2} \log fO_2 + \log K_2 + C$ (4)

456

457   in which C is an activity to wt% conversion factor, assumed constant. Equation 4

458   predicts a linear relationship between log Pt concentration and log fO$_2$, with a slope of ½,

459   as shown in Figure 5 for the results from Ertel et al (1999). In contrast to this previous

460   work involving Fe-free compositions, the variation in solubility with fO$_2$ determined here

461   shows some curvature, with the slope lessening with decreased fO$_2$. This effect could

462   result from two factors: first there may be an increased contribution from Pt particle

463   contamination to the abundance measurements, thus overestimating values at lower fO$_2$,

464   as well, the value of C may be changing due to the variation in the melt ferric/ferrous

465   ratio. In terms of the latter, the role of melt composition on the solubility of Pt has been

15

466 documented in previous work (Borisov and Danyushevsky, 2011; see Brenan et al. 2016,

467 page 27 for a detailed discussion), with solubility decreasing with an increased proportion

468 of network forming cations. The melt structural role of iron changes with fO_2, as ferric

469 iron is considered to have a network forming role, whereas ferrous iron is a network

470 modifier (Mysen et al., 1985; Dickenson and Hess, 1986). Ferric/ferrous ratios calculated

471 after the method of Kress and Carmichael (1991) for the experiments reported in this

472 study range from ~0.02 (FMQ-3.25) to ~1 (FMQ+5.5). Hence, increasing fO_2 results in a

473 higher portion of network forming ferric iron, increasing the value of C with increased

474 fO_2, thereby suppressing the increase in solubility that would occur if there were no melt

475 composition effect. Laurenz et al (2010) have also documented a similar change in slope

476 for the variation in Pd solubility with fO_2 as determined for FeO-bearing silicate melt.

477 Their suggested origin for this behaviour involves the stabilization of oxidized Pd^{2+}

478 species by reaction of Pd^{1+} with Fe^{3+}. This mechanism does not seem applicable,

479 however, to the case for Pt. Whereas both Pd^{1+} and Pd^{2+} have been documented to be

480 stable melt species based on Pd solubility in Fe-free compositions (Borisov et al, 1997),

481 Pt^{2+} is the only oxidation state inferred for Pt (with the exception of small amounts of Pt^{4+}

482 possible at highly oxidized conditions; Ertel et al., 1999), so the needed redox couple

483 involving different Pt species does not exist.

484

485 **Estimation of arsenic speciation in run-product glasses from solubility relations**

486   The concentration of arsenic in run-product glasses saturated in a Pt-arsenide melt

487 increases from a ~ 10 ppm at FMQ-3.25 to ~14 wt% at FMQ+5.4. This increase in

488 arsenic solubility is consistent with a dissolution reaction of the form:

489

490 $\text{As}_{(\text{Pt-arsenide})} + n/4 O_{2(\text{gas})} = \text{AsO}_{n/2(\text{silicate melt})}$ (5)
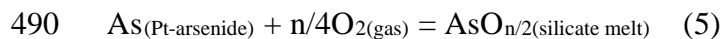
491

492 In which $\text{As}_{(\text{Pt-arsenide})}$ and $\text{AsO}_{n/2(\text{silicate melt})}$ are the dissolved arsenic species in the

493 arsenide and silicate melts, respectively. The equilibrium constant for this reaction is:

494

495 $K_5 = [\text{AsO}_{n/2(\text{silicate melt})}]/[\text{As}_{(\text{Pt-arsenide})}] \, fO_2^{n/4}$ (6)

496

497   which can be linearized to the form:

498

499   $\log K_5 = \log [AsO_{n/2(silicate\ melt)}] - \log [As_{(Pt-arsenide)}] - n/4 \log fO_{2(gas)}$ (7)

500

501   and solving for $\log [AsO_{n/2(silicate\ melt)}]$ yields:

502

503   $\log [AsO_{n/2(silicate\ melt)}] = \log [As_{(Pt-arsenide)}] + n/4 \log fO_{2(gas)} + \log K_5$ (8).

504

505   If the speciation of arsenic in the silicate melt remains constant over the fO_2 range

506   studied, and for a fixed $[As_{(Pt-arsenide)}]$, a plot of $\log [AsO_{n/2(silicate\ melt)}]$ vs. $\log fO_2$ will

507   yield a straight line with a slope of n/4. In this study, the arsenic content of the Pt-

508   arsenide melt varied between the extremes of equilibrium with sperrylite ($PtAs_2$) and Pt

509   metal. According to the Pt-As phase diagram, this corresponds to ~23 and ~8 wt% (43

510   and 18 at%) As for the melts coexisting with $PtAs_2$ and Pt, respectively. Arsenic

511   concentrations in the silicate melt are compared on an "isoactivity" basis by normalizing

512   molar abundances to unit activity by dividing by the mole fraction of arsenic in the

513   arsenide melt (i.e., assumes ideal mixing). Concentrations normalized in this manner are

514   displayed as a function of $\log fO_2$ in Figure 7. The slope of the weighted best-fit line to

515   these data is 0.502 (±0.001; r = 0.989), implying an arsenic valence state of +2.01. This

516   is an unusually low value for the arsenic cation, as previous studies of arsenic speciation

517   in silicate melt have suggested values of 3+, in addition to the neutral species (Borisova

518   et al., 2010; Chen and Jahanshahi, 2010).

519   As noted for the Pt solubility data, estimating redox state from solubility-fO_2

520   relations is complicated in Fe-bearing compositions, as Fe may affect the melt structure

521   in different ways, depending on valence state. Chen and Jahanshahi (2010) showed that

522   the activity coefficient for As_2O_3 in Fe-bearing slags (γ_{As2O3}) increased with fO_2, which

523   was interpreted to result from the increased proportion of network-forming ferric iron.

524   As described above, there is a large change in the proportion of ferric iron in melts

525   produced over the range of fO_2 investigated, suggesting that γ_{As2O3} will vary as well.

526   Using the Chen and Jahanshahi (2010) values for γ_{As2O3}, the solubility data have been

527   corrected for this effect, and also displayed in Figure 7. The weighted best-fit slope for

528 the activity-corrected data is 0.679 (+/- 0.001; r = 0.994), consistent with a valence state

529 of +2.72, or ~+3. Although the study of Chen and Jahanshahi (2010) focused on silicate

530 melt compositions appropriate for mineral processing (i.e., smelter slag), their work did

531 investigate the effect of other melt composition parameters, notably SiO_2 content. An

532 important result was that values of γ_{As2O3} increased with melt SiO_2 content, implying that

533 the arsenic content of the silicate melt required for arsenide saturation would

534 correspondingly decrease. Significantly, results also showed that although the absolute

535 value of γ_{As2O3} was found to increase with melt SiO_2, the relative change in γ_{As2O3} with

536 fO_2 did not. Another factor that might complicate this analysis is changes in the melt

537 composition as a result of increased As concentration in the melt with increased fO_2. For

538 experiments done at fO_2 greater than FMQ + 3, the As content of the silicate melt

539 significantly exceeds ~1 wt%, so in addition to changes in melt Fe^{3+} content, the high

540 levels of As may also effect the activity coefficient. Considering the relations shown in

541 Figure 7, there does not seem to be any systematic deviation from the regression line for

542 samples at ~1 wt% As and below. In fact, removing the three samples with As contents

543 greater than ~1 wt% from the regression improves the fit and increases the slope to 2.83,

544 such that the implied valence state is even closer to 3.   Hence, the conclusion that the

545 solubility-fO_2 relations supports a 3+ valence state in the silicate melt seems robust.

546   Although the L-edge XANES spectra also support the predominance of As^{3+} in

547 the melt, these measurements were done on glasses, quenched from the melt phase. Past

548 experimental work has shown that, in the presence of Fe, the speciation of some elements

549 can be altered during the quenching process (e.g., Cr; Berry et al., 2003; Berry and

550 O'Neill, 2004), specifically, oxidation of reduced species by reaction with Fe^{3+}. For the

551 case of the two most likely oxidation states of As, 3+ and 5+, that reaction would take the

552 form:

553

554 $$As^{3+} + 2\ Fe^{3+} = As^{5+} + 2\ Fe^{2+} \qquad (9)$$

555

556 Using the standard state free energy data for the pure oxides (Barin, 1995) the

557 equilibrium constant for this reaction is calculated to be ~10^{-8} at 1200°C, and decreases

558 with cooling, implying that oxidation of As^{3+} by this mechanism would be negligible.

18

559   Hence, results from both the solubility-fO_2 relations and XANES measurements indicate

560   the predominance of As^{3+} in the melts produced in this study. Borisova et al (2010) also

561   reported evidence for As^{3+} in a peralkaline rhyolitic glass (Macasuni, Peru), containing

562   ~410 ppm As, based on K-edge XANES. Their data suggest As dissolution in the form

563   of $AsO(OH)_2$ and/or $As(OH)_3$, based on the interpretation of the x-ray absorption fine-

564   edge structure (XAFS). Such results are certainly valid for hydrous melts, however,

565   experiments done in this study were anhydrous, so other dissolution mechanisms are

566   required. Combining their data with past work, Chen and Jahanshahi (2010) found that

567   γ_{As2O3} increased with melt SiO_2 content, implying strong interaction between As and the

568   other melt components, CaO and FeO, although the exact melt species was unspecified.

569   A fuller description of As dissolution in anhydrous silicate melt awaits future work.

570

571   **Geological implications and conclusions**

572   Two important observations derived from the experiments done in this study are:

573   1) The addition of arsenic to a magmatic system makes it possible to saturate in a Pt-

574   bearing phase at much lower Pt concentrations in the silicate melt (e.g., approximately 8-

575   fold for sperrylite saturation). This is due to the lower [Pt] represented by that phase, and

576   the lack of any effect of dissolved arsenic on enhancing Pt solubility. 2) However, the

577   amount of As required in the silicate melt to achieve Pt-arsenide saturation is in fact quite

578   high. Factors that may decrease the solubility of the Pt-arsenide phase are a reduction in

579   fO_2, and based on the previous work of Chen and Jahanshahi (2010), an increase in melt

580   SiO_2 content. Some of these aspects are summarized in Figure 8, which portrays the Pt

581   and As levels in basalt melt required for sperrylite saturation as a function of fO_2 relative

582   to FMQ. Bear in mind that the saturation curves presented are estimates at best,

583   particularly for Pt, as only one experiment successfully saturated the melt in sperrylite at

584   fO_2 high enough to reliably measure the Pt concentration. The assumption is that the Pt

585   content of the melt at sperrylite saturation parallels the solubility curve for pure Pt, but is

586   offset to lower values accounting for the reduced [Pt] in the saturating phase. The As

587   solubility curve is calculated from the Pt-arsenide solubility data presented in this study,

588   with the fO_2 dependence assuming an As^{3+} melt species, corrected for the change in

589   γ_{As2O3} with fO_2 as determined by Chen and Jahanshahi (2010). For a typical range in

terrestrial mafic magma fO$_2$ of FMQ-2 to FMQ, levels of Pt required for sperrylite saturation are 0.5 to 1 ppb, similar to average MORB (~1.5 ppb; Jenner and O'Neill, 2012), and in fact somewhat below levels measured in more Pt-enriched magmas, such as the Bushveld B3 composition (12 ppb, Barnes et al., 2010). In contrast, As concentrations required for sperrylite saturation are ~50-500 ppm over the same range of fO$_2$, >100x higher than levels in MORB, even at the reduced end of typical magmatic fO$_2$ (FMQ-2). Assuming that MORB is an adequate representation of the As content of mantle-derived magmas, results would therefore suggest that in order to achieve saturation in a Pt-arsenide phase at the magmatic stage requires the addition of arsenic from an external source, with reduction and addition of a siliceous component as other contributing factors. Of the choices of possible additives, it would seem that black shales may constitute an optimal contaminant to induce sperrylite saturation, owing to both their extreme enrichment in As (Figure 8), and also to the presence of organic-derived carbon, which could serve as a potent reductant, lowering the level of As (and Pt) required for saturation.

Hence, the most likely scenario for Pt-arsenide saturation would involve crustal contamination of arsenic-rich lithologies, and this is likely to be true for other arsenide phases considered to be primary, such as Fe-Ni-rich arsenide melt, as similar speciation in the silicate melt is expected. Some evidence for crustal contamination is evident in all the magmatic arsenide occurrences described in the introduction, with implication of arsenic-rich compositions, and reducing components, including organic-rich sediments, in some cases (Kylmakoski, Finland, Gervilla et al., 1998; Rosie Ni Prospect, Western Australia, Godel et al., 2012). This is also supported by the strong spatial association of arsenic-bearing PGMs in the Sudbury, Ontario deposits to the South Range ores, whose country rock includes As-bearing Huronian Supergroup sediments, relative to the As-poor Archean Levack Gneiss complex of the Superior-province in the North Range (Ames and Farrow 2007). As mentioned in the introduction, detailed chemical imaging has also revealed textural evidence favouring the direct crystallization of Pt-Fe alloy along with sperrylite from the magma that formed the orthopyroxenite section of the Monts de Cristal Complex (Gabon; Maier et al., 2015; Barnes et al 2016). Although preliminary modelling has suggested an origin for the complex involving assimilation of

a local granite, this material would have to be unusually As-rich to reach the required saturation level for sperrylite to form. There is no evidence for reduction of the parental magma to the complex, based on inferences from V in orthopyroxene (Barnes et al., 2016), likely ruling out interaction with a carbonaceous black shale contaminant. In the context of the data presented in this study, it is therefore not clear what factors could have lead to crystallization of sperrylite at the magmatic stage. One possibility not investigated in the current work is that the silicate melt composition has played a role in increasing [As] to a level allowing sperrylite saturation. As mentioned previously, Chen and Jahanshahi (2010) have documented a significant increase in $\gamma_{As_2O_3}$ with increasing melt silica content, indicating that melts with higher silica activity will require less arsenic to achieve saturation. In this context, it is of interest to note the high silica activity implied by the preponderance of orthopyroxenite cumulates in the Monts de Cristal Complex. Therefore, barring any unusual As-enrichment in the parental magma to the complex, perhaps increased silica activity may have played a role to induce sperrylite saturation, an effect that deserves further investigation.

Figure Captions

Figure 1. Backscattered electron images showing the textural development in the Pt-As phase assemblage from experimental run-products. All samples are surrounded by silicate melt, which is black owing to its low relative atomic number. In each of these experiments, the initial Pt-As phase assemblage was $PtAs_2$ + PtAs melt. A) Experiment M2SP13 containing Pt-Fe alloy + PtAs melt; B) Experiment M2SP4 containing PtAs

21

652 melt only; C) Experiment M2SP8 containing PtAs melt coexisting with stable $PtAs_2$

653 crystals.

654

655 **Figure 2.** Pt-As phase diagram determined at 0.1 MPa after Okamoto (1990), along with

656 the composition of PtAs melt produced in experiments. Note that the composition of

657 PtAs melt coexisting with either sperrylite (half-filled box) or Pt metal (half-filled

658 diamond) plots off the appropriate liquidus curves. However, both compositions are

659 nearly the same as the eutectic, consistent with quench crystallization of the stable solid

660 driving the liquid to the eutectic composition.

661

662 **Figure 3.** Time-resolved spectrum for glasses produced in experiments M2-SP5 (Pt-

663 saturated, As-free, filled triangles) and M2-SP8 ($PtAs_2$-saturated, filled and open

664 squares), both done at FMQ + 4.3. Concentrations of Pt and As in the glass are as

665 indicated.

666

667 **Figure 4.** Analytical traverses for arsenic (A) and platinum (B) from near the glass-

668 vapour interface (x = 0) to the bottom of the sample capsule reveal homogeneity for

669 samples synthesized over a large range in fO_2 (values correspond to ΔFMQ; in 1A),

670 result at FMQ + 4.3 is divided by 15 to prevent overlap.

671

672 **Figure 5.** Variation in platinum concentration in the silicate melt as a function of oxygen

673 fugacity for experiments saturated in Pt-Fe alloy (+/- As in silicate melt), Pt-As melt and

674 sperrylite ($PtAs_2$). Glass concentrations for experiments containing Pt-Fe alloy are

675 normalized to unit activity of platinum, using activity-composition relations in the alloy

676 summarized by Borisov and Palme (2000). The solid curve through the Pt data

677 corresponds to a weighted least-squares fit to a 2nd order polynomial. The anomalously

678 high solubility measured in experiment PtSol23 (ΔFMQ + 3) is excluded from the

679 regression. The dashed curve is a preliminary assessment of the solubility-fO_2 trend for

680 $PtAs_2$, and is simply offset from the Pt curve by the solubility of the one experiment

681 saturated in sperrylite. The dash-dot curve is the solubility-fO_2 relation determined for Pt

682 in the diopside-anorthite eutectic composition at 1300°C from Ertel et al (1999).

683

Figure 6. XANES spectra at the As L2,3-edge showing the relationship between normalized absorbance and energy (eV). Dashed vertical lines showing the As L2,3-edge binding energies reported in Thompson et al. (2009). Spectra have identical scales but are offset vertically for clarity.

Figure 7. Arsenic concentrations in the silicate melt as a function of ΔFMQ. Values are compared on an "isoactivity" basis by dividing concentrations (atomic ppm) by the mole fraction of arsenic in the arsenide melt (solid symbols). Open symbols are also corrected for the non-deal mixing of As^{3+} in molten silicate using the activity coefficients of Chen and Jahanshahi (2010). Slopes are weighted linear fits to the data. Symbols are the same as in Figure 5.

Figure 8. Estimated concentrations of Pt (blue) and As (gray and black) in basaltic magma at 1200°C required for saturation in sperrylite, $PtAs_2$. The model curve for Pt is taken from Figure 5. The curve for As is calculated from the activity of As in the silicate melt using the model of Chen and Jahanshahi (2010), scaled to the Pt-arsenide solubilities measured in this study, with an assumed 3+ speciation for As in the silicate melt (see text for more details). For reference are the Pt and As contents of MORB (Jenner and O'Neill, 2012), Pt content of Siberian picrite and Bushveld B3 magma (Lightfoot and Keays, 2005 and Barnes et al, 2010, respectively) and the As contents of average continental crust (Rudnick and Gao, 2004), as well as average and anomalous black shale (Ketris and Yudovich, 2009).

References

Ames D.E., Farrow C.E.G. (2007) Metallogeny of the Sudbury mining camp, Ontario. In: Goodfellow WD (ed) Mineral deposits of Canada: a synthesis of major deposit-types, district metallogeny, the evolution of geological provinces, and exploration methods. Geological Association of Canada, Special Publication No. 5, Mineral Deposits Division, pp 329–350.

714   Barin, I. (1995) *Thermochemical Data of Pure Substances*. VCH Publishers, New York.

715

716   Barnes, S.-J., Maier, W. D., Curl, W. A. (2010) Composition of the marginal rocks and

717   sills of the Rustenburg Layered Suite, Bushveld Complex, South Africa: Implications for

718   the formation of the platinum-group element deposits. *Econ. Geol.* **105**, 1491-1511.

719

720   Barnes, S.J., Fisher, L.A., Godel, B., Pearce, M.A., Maier, W.D., Paterson, D., Howard,

721   D.L., Ryan, C.G., Laird, J.S. (2016) Primary cumulus platinum minerals in the Monts de

722   Cristal Complex, Gabon: magmatic microenvironments inferred from high-definition X-

723   ray fluorescence microscopy. Contributions to Mineralogy and Petrology, vol 171, article

724   23.

725

726   Bennett, N., Brenan, J.M. and Koga, K.T. (2014) The solubility of platinum in silicate

727   melt under reducing conditions: Results from experiments without metal inclusions.

728   Geochimica et Cosmochimica Acta, vol 133, pp 422-442.

729

730   Benzerara, K., Morin, G., Yoon, T.H., Miot, J., Tyliszczak, T., Casoit, C., Bruneel, O.,

731   Farges, F. and Brown Jr., G.E. (2008) Nanoscale study of As biominealization in an acid

732   mine drainage system. Geochimica et Cosmochimica Acta, vol 72, pp 3949-3963.

733

734   Berry A.J., Shelley, J.M.G., Foran, G.J., O'Neill, H.St.C., Scott, D.R. (2003) A furnace

735   design for XANES spectroscopy of silicate melts under controlled oxygen fugacities and

736   temperatures to 1773 K. J. Synchrotron Rad., vol 10, pp. 332-336.

737

738   Berry A.J., and O'Neill, H.St.C. (2004) A XANES determination of the oxidation state of

739   chromium in silicate glasses. American Mineralogist, vol 89, pp 790-798.

740

741   Borisov A. and Danyushevsky L. (2011) The effect of silica content of Pd, Pt and Rh

742   solubilities in silicate melts: an experimental study. European Journal of Mineralogy, vol

743   23, pp 355-367

744

745 Borisov, A., Palme, H. (2000). Solubilities of noble metals in Fe-containing silicate melts

746 as derived from experiments in Fe-free systems. American Mineralogist, vol 85, pp

747 1665–1673.

748

749 Borisov, A. and Palme, H. (1997). Experimental determination of the solubility of

750 platinum in silicate melts. Geochimica et Cosmochimica Acta, vol 61, pp 4349-4357.

751

752 Borisova A.Y, Pokrovski, G.S., Pichavant, M., Freydier, R., Candaudapl, F. (2010)

753 Arsenic enrichment in hydrous peraluminous melts: Insights from femtosecond laser

754 ablation-inductively coupled plasma-quadrupole mass spectrometry, and in situ X-ray

755 absorption fine structure spectroscopy. American Mineralogist, vol 95, pp. 1095–1104.

756

757 Brenan, J.M., Bennett, N. and Zajacz, Z. (2016) Experimental results on fractionation of

758 the highly siderophile elements (HSE) at variable pressures and temperatures during

759 planetary and magmatic differentiation. Reviews in Mineralogy and Geochemistry, Vol

760 81, pp 1-88.

761

762 Canil, D. (1997). Vanadium partitioning and the oxidation state of Archaean komatiite

763 magmas. Nature vol 389, pp 842-845.

764

765 Canil, D. and Fedortchouk,Y. (2001) Olivine/liquid partitioning of vanadium and other

766 trace elements, with applications to modern and ancient picrites. Canadian Mineralogist

767 vol 39, pp. 319-330.

768

769 Chen C. and Jahanshahi, S. (2010) Thermodynamics of Arsenic in $FeOx$-CaO-SiO_2

770 slags. Metallurgical and Materials Transactions B, vol 41B, pp 1166-1174.

771

772 Dare Sarah A. S., Barnes S.J., Prichard H. M. (2010) The Timing and Formation of

773 Platinum-Group Minerals from the Creighton Ni-Cu-Platinum-Group Element Sulfide

774 Deposit, Sudbury, Canada: Early Crystallization of PGE-Rich Sulfarsenides. Economic

775 Geology vol 105, pp 1071-1096.

776

777 Dickenson M.P. and Hess, P.C. (1986) The structural role and homogeneous redox

778 equilibria of iron in peraluminous, metaluminous and peralkaline silicate melts.

779 Contributions to Mineralogy and Petrology, vol 92, pp 207-217.

780

781 Eggins, S.M., Kinsley, L.P.J., & Shelley J.M.M. (1998) Deposition and element

782 fractionation   processes during atmospheric pressure laser sampling for analysis by

783 ICPMS. Applied Surface Science, vol 127-129, pp. 278-286.

784

785 Ertel, W., O'Neill, H. St. C., Sylvester, P. J., Dingwell, D. B. (1999). Solubilities of Pt

786 and Rh in a haplobasaltic silicate melt at $1300°C$. Geochimica et Cosmochimica Acta, vol

787 63, pp 2439-2449.

788

789 Foster, A.L. and Kim, C.S. (2014) Arsenic Speciation in Solids Using X-ray Absorption

790 Spectroscopy. Reviews in Mineralogy & Geochemistry, vol 79, pp 257-369

791

792 Frost B.R., Mavrogenes J.A., Tomkins A.G. (2002) Partial melting of sulfide ore deposits

793 during medium- and high-grade metamorphism. Canadian Mineralogist vol 40, pp 1-18.

794

795 Gervilla F., Leblanc M., Torres-Ruiz J., and Fenoll H.P. (1996) Immiscibility between

796 arsenide and sulfide melts: a mechanism for the concentration of noble metals. Canadian

797 Mineralogist vol 34, pp 485-502.

798

799 Gervilla F., Papunen H., Kojonen K. and Johanson B. (1998) Platinum-, palladium- and

800 gold-rich arsenide ores from the Kylmäkoski Ni-Cu deposit (Vammala Nickel Belt, SW

801 Finland); Mineralogy and Petrology vol 64, pp 163-185.

802

803 Godel B, Gonzalez-Alvarez I, Barnes SJ et al (2012) Sulfides and Sulfarsenides from the

804 Rosie Nickel Prospect, Duketon Greenstone Belt, Western Australia. Economic Geology

805 vol 107, pp 275-294.

806

807   Hanley J. (2007) The role of Arsenic-rich melts and mineral phases in the development of

808   high grade Pt-Pd mineralization within komatiite-associated magmatic Ni-Cu sulfide

809   horizons at Dundonald Beach South, Abitibi Subprovince, Ontario, Canada. Economic

810   Geology vol 102, pp 305–317.

811

812   Helmy H.M., Ballhaus C., Fonseca R.O.C. and Nagel T.J. (2013) Fractionation of

813   platinum, palladium, nickel, and copper in sulfide–arsenide systems at magmatic

814   temperature. Contributions to Mineralogy and Petrology vol 166, pp 1725–1737.

815

816   Helmy H.M., Ballhaus C., Wohlgemuth-Ueberwasser C., Fonseca R.O.C., and Laurenz

817   V. (2010) Partitioning of Se, As, Sb, Te and Bi between monosulfide solid solution and

818   sulfide melt-Application to magmatic sulfide deposits. Geochimica et Cosmochimica

819   Acta vol 74, pp 6174-6179.

820

821   Jenner, F.E. and O'Neill, H.St.C. (2012) Analysis of 60 elements in 616 ocean floor

822   basaltic glasses. Geochemistry Geophysics Geosystems, Volume: 13 Article Number:

823   Q02005 DOI: 10.1029/2011GC004009

824

825   Jochum, K.P., Weis, U., Stoll, B., Kuzmin, D., Yang, Q.C., Raczek, I., Jacob, D.E.,

826   Stracke, A., Birbaum, K., Frick, D.A., Gunther, D. and Enzweiler, J. (2011)

827   Determination of Reference Values for NIST SRM 610-617 Glasses Following ISO

828   Guidelines. Geostandards and Geoanalytical Research, vol 35, pp 398-429.

829

830   Ketris M.P. and Yudovich, Ya. E. (2009) Estimations of Clarkes for Carbonaceous

831   biolithes: World averages for trace element contents in black shales and coals.

832   International Journal of Coal Geology vol. 78, pp 135–148.

833

834   Kress V.C. and Carmichael I.S.E. (1991) The compressibility of silicate liquids

835   containing Fe_2O_3 and the effect of composition, temperature, oxygen fugacity and

836   pressure on their redox states. Contributions to Mineralogy and Petrology, vol 108, pp

837   82-92.

838

839 Laurenz, V., Faunseca, R.O.C., Ballhaus, C. and Sylvester, P.J. (2010) Solubility of

840 palladium in picritic melts: 1. The effect of iron. Geochimica et Cosmochimica Acta vol

841 74, pp 2989–2998.

842

843 Lightfoot, P. C., Keays, R. R. (2005) Siderophile and chalcophile metal variations in

844 flood basalts from the Noril'sk region: Implications for the origin of the Ni-Cu-PGE

845 sulfide ores. *Econ. Geol.* **100**, 439-462.

846

847 Lowers, H.A., Breit, G.N., Foster, A.L., Whitney, J., Yount, J., Uddin, M.N., Muneem,

848 A.A. (2007) Arsenic incorporation into authigenic pyrite, Bengal Basin sediment,

849 Bangladesh. Geochimica et Cosmochimica Acta, vol 71, pp 2699-2717

850

851 Maier W.D., Rasmussen B., Fletcher I., Godel B., Barnes S.J., Fisher L., Yang S.H.,

852 Huhma H., Lahaye Y. (2015) Petrogenesis of the ~2.77 Ga Monts de Cristal Complex,

853 Gabon: evidence for direct precipitation of Pt-arsenides from basaltic magma. Journal of

854 Petrology, vol 56, pp 1285-1307.

855

856 Makovicky, E., Karup-Moller, S., Makovicky, M., Rose-Hansen, J. (1990) Experimental

857 studies on the phase systems Fe–Ni–Pd–S and Fe–Pt–Pd–As–S applied to PGE deposits.

858 Mineralogy and Petrology vol 42, pp 307–319.

859

860 Makovicky, E., Makovicky, M., Rose-Hansen, J., 1992. The phase system Pt–Fe–As–S at

861 850 ºC, and 470 ºC. Neues Jahrbuch fuer Mineralogie Monatshefte vol 10, pp 441–453.

862

863 Mallmann, G. & O'Neill, H. St.C. (2009). The crystal/melt partitioning of V during

864 mantle melting as a function of oxygen fugacity compared with some other elements (Al,

865 P, Ca, Sc, Ti, Cr, Fe, Ga, Y, Zr and Nb). Journal of Petrology vol 50, pp 1765-1794.

866

867 Medard, E., Schmidt, M.W., Wälle, M., Keller, N.S., Günther, D. (2015) Platinum

868 partitioning between metal and silicate melts: Core formation, late veneer and the

869 nanonuggets issue. Geochimica et Cosmochimica Acta, vol 162, pp 183-201.

870

871 Morin G., Juillot F., Casiot C., Bruneel O., Personne´ J. C., Elbaz-Poulichet F., Leblanc

872 M., Ildefonse P. and Calas G. (2003) Bacterial formation of tooeleite and mixed

873 arsenic(III) or arsenic(V)–iron(III) gels in the Carnoule`s acid mine drainage, France. A

874 XANES, XRD, and SEM study. Environmental Science and Technology, vol 37, pp

875 1705–1712.

876

877 Moulton, B.J.A., Henderson, G.S., Sonneville, C., O'Shaughnessy, C., Zuin, L., Regier,

878 T. and de Ligny, D. (2016) The structure of haplobasaltic glasses investigated using X-

879 ray absorption near edge structure (XANES) spectroscopy at the Si, Al, Mg, and O K-

880 edges and Ca, Si, and Al $L_{2,3}$-edges. Chemical Geology, vol 420, pp 213-230

881

882 Mysen, B.O., Virgo, D., Neumann, E-R, Siefert, F.A. (1985) Redox equilibria and the

883 structural states of ferric and ferrous iron in melts in the system $CaO-MgO-Al_2O_3-SiO_2$-

884 Fe-O: relationships between redox equilibria, melt structure and liquidus phase equilibria.

885 American Mineralogist, vol 70, pp 317-331.

886

887 Newville, M. (2001) IFEFFIT: Interactive XAFS analysis and FEFF fitting. Journal of

888 Synchrotron Radiation, vol 8, pp 322–324.

889

890 Okamoto, H. (1990) As-Pt (arsenic-platinum). Journal of Phase Equilibria, vol 17, pp

891 456.

892

893 Pina R, Gervilla F, Barnes S-J, Ortega L, Lunar R (2013) Partition coefficients of

894 platinum group and chalcophile elements between arsenide and sulfide phases as

895 determined in the Beni Bousera Cr–Ni mineralization (North Morocco). Econ Geol 108:

896 935–951

897

898   Ravel, B. and Newville, M. (2005) Athena, artemis, hephaestus: Data analysis for X-ray
899   absorption spectroscopy using IFEFFIT. Journal of Synchrotron Radiation, vol 12, pp
900   537–541.

901

902   Regier, T., Krochak, J., Sham, T.K., Hu, Y.F., Thompson, J., Blyth, R.I.R. (2007)
903   Performance and capabilities of the Canadian Dragon: The SGM beamline at the
904   Canadian Light Source. Nuclear Instruments and Methods in Physics Research Section
905   A – Accelerators Spectrometers Detectors and Associated Equipment, vol 582, pp 93-95.

906

907   Sinyakova EF and Kosyakov VI (2012) The behavior of noble-metal admixtures during
908   fractional crystallization of As- and Co-containing Cu–Fe–Ni sulfide melts. Russian
909   Geology and Geophysics vol 53, pp 1055–1076.

910

911   Skinner B.J., Luce F.D., Dill J.A., Ellis D.E., Hagan H.A., Lewis D.M., Odell
912   Tomkins, Andrew G.; Frost, B. Ronald; Pattison, David R. M. (2006) Arsenopyrite
913   melting during metamorphism of sulfide ore deposits. Canadian Mineralogist, vol 44, pp
914   1045-1062.

915

916   Sverjensky D.A., Williams N. (1976) Phase relations in ternary portions of the system Pt-
917   Pd-Fe-As-S. Economic Geology vol 71, pp 1469–1475.

918

919   Thompson, A., Attwood, D., Gullikson, E., Howells, M., Kim, K-J, Kirz, J., Kortright, J.,
920   Lindau, I., Liu, Y., Pianetta, P., Robinson, A., Scofield, J., Underwood, J. and Williams,
921   G. (2009) X-ray data booklet. Lawrence Berkeley National Laboratory, University of
922   California, Berkeley, CA 94720

923

924   Thoral S., Rose J., Garnier J. M., Van Geen A., Refait P., Traverse A., Fonda E., Nahon
925   D. and Bottero J. Y. (2005) XAS study of iron and arsenic speciation during Fe(II)
926   oxidation in the presence of As(III). Environ. Sci. Tech., vol 39, pp 9478–9485.

Table 1. Summary of As-bearing and related experiments and run-product compositions

expt ID	Buffer	log fO2	ΔFMQ	duration (hrs)	PtFe alloy	PtAs(melt)	PtAs2 (sperrylite)	SiO2	TiO2	Al2O3	FeO	MgO	CaO	Na2O	MnO	K2O	n	Total[4]	V (LA)	Pt (LA)	As (LA)	As (EPMA)	Fe	Pt	As	total	n	Fe	Ni	Pt	total	n	aPt alloy	ppm Pt
								silicate (wt%) by EPMA											ppm by LA-ICPMS			ppm by EPMA	arsenide(melt) (wt%)					alloy (wt%) by EPMA					2[Pt]=1	
PtSol14[1]	CO-CO2	-6.37	2.03	92.5	x			47.07	5.01	13.56	11.67	9.73	11.37	1.24	0.16	0.36	15	100.25		0.028								3.14	na	97.35	100.49	2	0.81	0.03
								0.33	0.16	0.12	0.20	0.13	0.14	0.04	0.05	0.02				0.008								0.12		0.34				0.01
Ptsol16a[1]	CO-CO2	-9.38	-0.98	95	x			46.74	5.05	13.73	11.31	8.83	11.54	1.32	0.16	0.39	13	99.18		<0.0047								7.79	na	92.32	100.11	9	0.29	<0.0047
								0.18	0.19	0.11	0.21	0.14	0.08	0.06	0.03	0.03												0.96		1.16				
PtSol21[1]	CO-CO2	-3.16	5.24	91	x			50.63	5.35	15.14	7.99	5.87	12.28	1.19	0.09	0.42	13	99.02		0.286								0.26	na	101.29	101.56	9	0.99	0.29
								0.34	0.25	0.14	0.10	0.09	0.19	0.07	0.04	0.03				0.072								0.05		0.56				0.07
PtSol22[1]	CO-CO2	-0.68	7.72	91.5	x			51.45	3.94	14.88	8.56	6.94	11.72	0.88	0.12	0.35	12	98.87		2.57								0.04	na	101.45	101.49	9	1.00	2.57
								0.17	0.16	0.11	0.18	0.08	0.14	0.05	0.03	0.03				1.00								0.01		0.64				1.00
PtSol23[1]	CO-CO2	-5.39	3.01	90	x			47.76	4.99	13.96	10.02	8.51	11.86	1.37	0.15	0.42	15	99.10		0.129								1.15	na	100.39	101.55	10	0.95	0.14
								0.34	0.16	0.12	0.13	0.09	0.13	0.08	0.04	0.03				0.016								0.25		0.37				0.02
PtSol37[1]	CO-CO2	-1.61	6.79	96	x			54.11	4.53	14.46	7.32	4.20	13.48	1.19	0.06	0.43	15	99.86		1.71								0.08	<0.01	99.49	99.57	9	1.00	1.71
								0.27	0.27	0.19	0.23	0.09	0.19	0.06	0.04	0.03				0.09								0.02		0.57				0.09
PtSol38[1]	CO-CO2	-3.13	5.27	95	x			51.10	5.47	12.76	9.09	6.31	12.83	1.49	0.10	0.45	15	99.66		0.405								0.34	<0.01	99.31	99.66	8	0.99	0.41
								0.26	0.18	0.11	0.17	0.08	0.13	0.08	0.04	0.03				0.033								0.02		0.61				0.03
PtSol39[1]	CO-CO2	-3.23	5.17	46.00	x			52.22	5.36	13.64	7.89	6.10	12.44	1.43	0.08	0.41	13	99.69		0.342								0.37	<0.01	99.39	99.76	9	0.99	0.35
								0.34	0.25	0.11	0.17	0.11	0.09	0.07	0.04	0.02				0.031								0.06		0.74				0.03
PtSol40[1]	CO-CO2	-0.68	7.72	93.50	x			52.78	2.92	14.27	9.01	6.44	12.30	1.28	0.11	0.43	14	99.56		5.04								0.10	<0.01	99.54	99.63	6	1.00	5.06
								0.32	0.18	0.12	0.25	0.10	0.16	0.06	0.04	0.03				0.51								0.03		0.58				0.51
SP7	MnO-Mn3O4	-4.10	4.30	87.33	x			47.74	5.71	16.08	8.66	5.12	11.68	0.59	0.10	0.22	15	97.84	410.19	0.171	14684							1.17	0.05	97.93	99.14	7	0.95	0.181
								0.58	1.57	4.75	2.01	1.34	1.76	0.08	0.04	0.05			73.29	0.035	1681							0.04	0.01	0.63				0.037
SP11[1]	Ni-NiO	-7.72	0.68	94.50	x			46.18	5.19	15.54	11.60	8.44	11.35	0.56	0.17	0.17	14	99.19	32.65	0.011	<1							7.00	0.65	91.48	99.14	10	0.53	0.021
								0.37	0.21	0.18	0.24	0.11	0.14	0.05	0.04	0.02			0.97	0.005								0.16	0.03	0.66				0.009
SP12[1]	Mo-MoO2	-11.65	-3.25	94.50	x			48.47	4.93	15.23	10.33	7.89	11.31	0.86	0.18	0.25	14	99.45	10.80	0.053	<1							19.09	1.67	76.95	97.71	2	0.11	0.500
								0.34	0.18	0.12	0.21	0.11	0.09	0.05	0.05	0.03			0.12	0.012								0.40	0.05	0.38				0.113
SP14	MnO-Mn3O4	-4.10	4.30	48.00	x			46.46	5.31	15.40	10.53	6.87	11.02	0.52	0.16	0.18	8	97.81	260.48	0.188	10385							1.34	0.07	97.58	99.00	10	0.93	0.201
								0.24	0.20	0.20	0.20	0.14	0.10	0.04	0.05	0.04			63.94	0.044	504							0.08	0.02	0.53				0.047
M2-SP3[1]	Ni-NiO	-7.72	0.68	96.00	x			47.71	5.28	15.27	10.88	8.82	12.06	0.48	0.19	0.12	10	100.82	34.77	0.008	<1							7.44		91.02	98.46	4	0.51	0.016
								0.12	0.17	0.06	0.11	0.10	0.17	0.03	0.03	0.02			0.31	---								0.06		1.04				---
M2-SP4[3]	Ni-NiO/no buffer	-7.72/-7.7	0.68/0.7	96.00		x		47.52	5.00	15.02	11.58	8.79	11.86	0.44	0.19	0.08	9	100.47	34.56	0.006		820	1.93	73.82	24.23	100.00	7							
								0.21	0.19	0.11	0.19	0.09	0.15	0.06	0.04	0.02			0.36	---		7	0.03	0.41	0.40									
M2-SP5[1]	MnO-Mn3O4	-4.10	4.30	96.00	x			50.69	6.04	14.38	9.37	5.88	11.90	0.44	0.11	0.16	9	98.96	348.83	0.091	<1							4.26		95.77	100.03	14	0.74	0.123
								0.40	0.18	0.09	0.19	0.07	0.16	0.04	0.03	0.03			60.16	0.030								0.25		0.52				0.040
M2-SP6[3]	MnO-Mn3O4/no buffer	-4.1/-4.8	4.3/3.6	96.00		x		49.58	5.74	14.64	9.19	6.03	12.03	0.91	0.12	0.14	9	100.28	200.69	0.040		14377	0.25	74.36	25.39	100.00	4							
								0.40	0.23	0.13	0.15	0.07	0.05	0.06	0.03	0.04			2.67	0.019		804	0.06	0.56	0.54									
M2-SP7[1]	CO-CO2	-7.72	0.68	96.00	x			45.43	5.23	15.18	11.52	8.46	12.15	1.45	0.17	0.00	15	100.18	36.32	0.006	<1							8.46		92.75	101.20	8	0.46	0.012
								0.15	0.07	0.29	0.15	0.11	0.11	0.04	0.02	0.00			0.38	0.003								0.46		0.78				0.007
M2-SP8[3]	CO-CO2/no buffer	-7.72/-4.1	0.68/4.3	92.50		x	x	43.27	5.00	15.12	9.04	6.06	11.73	0.53	0.13	0.13	15	98.60	337.34	0.020	57489	69224	nd	84.55	15.45	100.00	1							
								0.20	0.06	0.15	0.12	0.08	0.06	0.03	0.02	0.01			3.43	0.002	1271	758												
M2-SP9[3]	CO-CO2/no buffer	-7.72/-3.0	0.68/5.4	92.50		x		45.26	6.00	15.22	7.69	4.96	12.22	0.53	0.11	0.14	13	98.40	862.17	0.062	47596	58963	nd	81.00	19.00	100.00	1							
								0.48	0.16	0.27	0.25	0.10	0.13	0.05	0.01	0.01			10.57	0.016	629	1228												
M2-SP13[3]	CO-CO2/no buffer	-7.72/-7.1	0.68/1.3	98.50	x		x	46.91	6.19	15.72	7.12	9.62	13.30	1.01	0.15	0.26	11	100.54	46.78	0.0067		834	nd	85.40	14.60	100.00	1	5.07		95.78	100.84	9	0.68	0.0098
								0.31	0.36	1.21	0.40	0.58	0.37	0.05	0.03	0.02			0.70	0.0003		18						0.02		0.29				0.0005
M2-SP21	Mo-MoO2	-11.65	-3.25	48.50	x		x	46.71	5.70	15.38	8.86	9.40	12.95	1.11	0.14	0.28	15	100.65	10.47	0.0163	6.5							20.14		79.77	99.90	10	0.09	0.18
								0.26	0.07	0.14	0.09	0.09	0.09	0.04	0.02	0.02			0.39	0.0035	1.7							0.13		0.46				0.04
M2-SP28[3]	CO-CO2/no buffer	-3/-2.9	5.4/5.5	90.00		x		42.03	3.86	15.44	5.31	1.94	9.60	0.48	0.08	0.17	15	98.10	983.38	1.67	-	145362	nd	88.64	9.71	98.40	8							
								0.85	0.15	0.15	0.21	0.08	0.14	0.03	0.02	0.02			50.19	0.13	-	2776		0.53	0.42									

1) Pt-saturated, As-free experiments

2) Value corrected to unit activity of Pt calculated from the Pt content of the metal phase

3) two-step experiment, see text for details

4) glass total also includes As calculated as As2O3. Note also that low totals for experiments done at high fO2 indicates the presence of Fe3+

nd = not detected

na = not analysed

values in italics represent 1 standard deviation of n analyses

All experiments were done at 1200°C

Figure